Selective nanoparticle heating: Another form of nonequilibrium in dusty plasmas

Lorenzo Mangolini and Uwe Kortshagen

Department of Mechanical Engineering, University of Minnesota, 111 Church Street SE, Minneapolis, Minnesota 55455, USA

Nanoparticles produced in low-temperature plasmas (LTPs) are often found with crystalline structure, which suggests rather high temperatures during synthesis. This even applies to particles of high-melting-point materials, which is surprising, because the gas temperature in LTPs is often close to room temperature and particles may reside in the plasma only for a few milliseconds. In this paper, we present a numerical study of nanoparticle heating in plasmas through energetic surface reactions. We find that, under realistic plasma conditions, particle temperatures can exceed the gas temperature by many hundreds of kelvins. However, as the particle temperature is highly unsteady, it is more reasonable to consider particle temperature distribution functions. The dependence of the particle temperature distribution on particle size and particle density in a dusty LTP is discussed.

I. INTRODUCTION

Chemically active low-temperature plasmas (LTPs) have been known to be efficient sources of nanoparticle formation for quite a while [1]. In many experiments, it was observed that the nanoparticles formed in the plasma are crystalline in nature [2–7], which—depending on the nanoparticle material—suggests rather high temperatures during the particle formation. For instance, studies in [8] suggested that the crystallization temperature of silicon particles is diameters of 4, 6, 8, and 10 nm are 773, 1073, 1173, and 1273 K, respectively. Crystallization temperatures of 1047 K and higher were reported for silicon particles larger than 10 nm in [9].

These relatively high temperatures required for the crystallization of nanoparticles reveal a persistent puzzle for the formation of crystalline nanoparticles in LTPs in that crystallization temperatures are often significantly higher then the gas temperatures in LTPs, yet nanocrystals are consistently found. For instance, in Ref. [5] nanocrystals of silicon were formed in a flowthrough-type plasma setup, in which the nanoparticles reside in the plasma for only a few milliseconds (typically 2–6 ms). The gas temperatures measured in this reactor were between 420 and 520 K [5], significantly lower than the crystallization temperatures reported for small silicon nanocrystals.

Several researchers have pointed out in the past that the temperatures of particles immersed in plasmas can exceed the gas temperature. Daugherty and Graves used spectroscopic fluoresencent measurements to determine the temperatures of 0.5–3 μm particles in a capacitively coupled radio-frequency discharge [10]. They found particle temperatures exceeding the gas temperature by about 75 K and proposed an energy balance for the particles taking into account particle heating through election-ion recombination and cooling through radiation and conduction. Similar results were reported by Swinkels *et al.* [11], who studied the fluorescence emission of rhodamine-B-dyed particles with diameters of 2.4 μm. Particle temperatures up to 450 K were also found in [12]. In [13] we had argued that nanoparticles are heated to significantly higher temperatures than had been observed in previous studies of micrometer-sized particles.

The fact that we found cubic shaped silicon nanocrystals with $\langle 100 \rangle$ faces suggested that particles had been heated to temperatures that allowed them to attain their equilibrium shape for hydrogen-terminated silicon crystals [14]. We discussed that particles needed to be heated to temperatures of several hundreds of kelvins above the gas temperature to undergo the observed transition from agglomerates of amorphous particles to well-formed, cube-shaped single crystals of 35 nm diameter. In [5] we used a simple simulation, only accounting for electron-ion recombination at the particle surface, to show that the temperature of small particles below 10 nm in size is highly unsteady and can exceed the temperature of the surrounding gas by $\sim$600 K.

In this paper, we present a comprehensive numerical model to describe the temperature of small nanoparticles in plasmas. Since the formation of silicon particles in silane plasmas is the most widely studied system in the literature, we focus on this problem even though the presented formalism can easily be transferred to other nanoparticle materials and precursor gases. As the temperature of small particles is found to be highly unsteady, we introduce the concept of a particle temperature distribution function. We apply this model to the plasma situation studied in [5]. We also discuss the effect of particle concentration on the particle temperature distribution.

The paper is organized as follows. The numerical model is introduced in Sec. II. Section III describes experimental studies on the system described in [5] which were used to determine realistic values for input parameters for the model. Section IV presents results and their discussion. Conclusions are summarized in Sec. V.

II. MODEL DESCRIPTION

In this work a nonsteady formulation of the particle energy balance is used:

$$\frac{4}{3}\pi r_p^3 \rho C \frac{dT_p}{dt} = G - L, \tag{1}$$

where ρ is the density of silicon and C is its specific heat, r_p and T_p are the particle radius and temperature, respectively,

G is a heat generation term, and L is the heat sink term. The mass density and specific heat of silicon nanoparticles are assumed to be equal to those of the bulk material, and particles are assumed to be spherical. It is also assumed that the particle temperature equilibrates instantaneously throughout the particle, since solid state heat transfer is significantly faster than the other heat transfer processes considered. The equation is discretized using a typical time step of 10^{-10} s. The term L is calculated as

$$L = \frac{1}{4} n_{\text{gas}} S \sqrt{\frac{8k_B T_{\text{gas}}}{\pi m_{\text{gas}}}} \times \frac{3}{2} k_B (T_p - T_{\text{gas}}). \qquad (2)$$

This term represents the heat conduction losses to the background gas, which is assumed to be argon in this paper. n_{gas} is the background gas density, T_{gas} is the background gas temperature, S is the particle surface area $4\pi r_p^2$, m_{gas} is the atomic mass of the background gas, k_B is the Boltzmann constant, and T_p is the particle temperature. This term is implemented in the model using a continuous, i.e., nonstochastic, approach, since the collision frequency between the particle and the background gas atoms is much larger than the collision frequency with ions and radicals. The background gas temperature is assumed to be equal to 300 K, which is a reasonable approximation for LTPs at low power density. Radiation is neglected as the time scale for radiative cooling of nanoparticles is longer than the time scale for conductive cooling for the particle temperatures observed in this study [15].

The generation term G in Eq. (1) describes the heat released by recombination and chemical reactions at the particle surface. For the case of silicon particles produced in a silane plasma with a surplus of hydrogen, we here consider electron-ion recombination at the particle surface and hydrogen surface reactions. In Ref. [16] we studied the charging of particles and found that, for very small nanoparticles with diameters smaller than 10 nm, the orbital-motion-limited (OML) theory is a good assumption. The collision frequency between particles and charged species within the OML theory is given by [17]

$$\nu_{e,i}$$
$$= \begin{cases} n_{e,i} S \sqrt{\dfrac{k_B T_{e,i}}{2\pi m_{e,i}}} \exp\left(-\dfrac{q_{e,i}\Phi}{k_B T_{e,i}}\right), & q_{e,i}\Phi \geq 0, \qquad (3a) \\[2ex] n_{e,i} S \sqrt{\dfrac{k_B T_{e,i}}{2\pi m_{e,i}}} \left(1 - \dfrac{q_{e,i}\Phi}{k_B T_{e,i}}\right), & q_{e,i}\Phi < 0, \qquad (3b) \end{cases}$$

where $\nu_{e,i}$ is the collision frequency of a particle with an electron or an ion, respectively, $n_{e,i}$ is the electron (ion) density, $m_{e,i}$ is the electron (ion) mass, $q_{e,i}$ is the electron (ion) charge, $T_{e,i}$ is the electron (ion) temperature, and Φ is the particle potential, calculated as

$$\Phi = \frac{eZ}{4\pi\varepsilon_0 r_p}. \qquad (4)$$

Z is the number of elementary charges on the particle, e is the elementary charge, and ε_0 is the vacuum dielectric constant. The ion temperature is assumed to be equal to the background gas temperature.

The collisions with charged species are implemented using a stochastic model, following the example in [18]. First, the time between two collisions Δt_{charge}, without differentiating between collisions with an ion or with an electron, is calculated as

$$\Delta t_{\text{charge}} = -\frac{\ln(r_1)}{\nu_e + \nu_i} \qquad (5)$$

with r_1 a random number between 0 and 1. Another random number is then selected to choose whether the collision is with an electron or with an ion:

$$\text{if } r_2 < \frac{\nu_e}{\nu_e + \nu_i} \quad \text{then } Z = Z - 1, \qquad (6a)$$

$$\text{else } Z = Z + 1, \qquad (6b)$$

with r_2 also randomly chosen between 0 and 1. The simulation keeps track of the particle charge and potential, and the collision frequencies with ions and electrons are updated at every charging event using Eq. (3). In the case of collision with an ion, the particle charge increases by one unit, recombination takes place, and an argon atom is desorbed from the surface in its ground state. The energy released in this case is equal to the ionization potential for argon, 15.76 eV.

The collisions with atomic hydrogen are also modeled in a stochastic way. The collision frequency and time between collisions are given by

$$\nu_{\text{H}} = \frac{1}{4} n_{\text{H}} S \sqrt{\frac{8k_B T_{\text{H}}}{\pi m_{\text{H}}}}, \qquad (7a)$$

$$\Delta t_{\text{H}} = -\frac{\ln(r_3)}{\nu_{\text{H}}}, \qquad (7b)$$

where n_{H} is the atomic hydrogen density, m_{H} is the atomic mass of hydrogen, and T_{H} is the hydrogen temperature, also assumed to be equal to the background gas temperature. ν_{H} is the particle collision frequency with atomic hydrogen. r_3 is another random number between 0 and 1, and Δt_{H} is the time between collisions of a particle with a hydrogen radical.

A collision between atomic hydrogen and the particle surface can lead to different energy transfer mechanisms depending on the fractional hydrogen surface coverage. An incoming hydrogen atom has a 100% probability of reacting with a surface dangling bond. This pathway is stochastically selected by comparing random number r_4 with the fractional hydrogen surface coverage f_S:

$$\text{if } r_4 > f_S \quad \text{then } N_{\text{H}} = N_{\text{H}} + 1. \qquad (8)$$

The fractional hydrogen coverage f_S is equal to the number of hydrogen surface atoms N_{H} divided by the number of available hydrogen surface sites. Since hydrogen can bond to silicon via mono-, di-, and trihydride bonds, we assume that on average two hydrogen atoms are bonded to every surface silicon atom. The number of silicon surface atoms as a function of size is calculated using the relation given in Ref. [1], p. 89. The reaction of a hydrogen atom with a dangling bond releases 3.1 eV, equal to the binding energy of the Si-H

bond. If a hydrogen radical lands on the hydrogen-terminated fraction of the surface, a new random number r_5 is generated and compared to the probability of hydrogen-induced abstraction through the Eley-Rideal mechanism [19]:

$$\text{if } r_5 < P_{abs} \text{ then } N_H = N_H - 1. \qquad (9)$$

Here r_5 is another random number between 0 and 1. The probability of hydrogen-induced abstraction, P_{abs}, is equal to 11%, and the heat released in this case is equal to the bond energy of the hydrogen molecule (4.51 eV) diminished by the energy of the broken Si-H bond (3.1 eV), giving a net energy release of 1.41 eV. In the remaining 89% of cases, hydrogen is physisorbed and diffuses along the particle surface. In this case, we calculate the time necessary for the hydrogen atom to diffuse and reach a surface dangling bond using the following relations:

$$D = D_0 \exp(-E_D/k_B T_p), \qquad (10a)$$

$$L_D = \frac{1}{2} L_{\text{Si-Si}} \frac{1}{(1 - f_S)}, \qquad (10b)$$

$$\nu_D = \frac{D}{L_D^2}, \qquad (10c)$$

$$\tau_D = -\frac{\ln(r_6)}{\nu_D}. \qquad (10d)$$

The diffusion coefficient D of atomic hydrogen on a hydrogen-terminated silicon surface follows an Arrhenius expression with a small activation energy E_D equal to 0.1 eV and a preexponential factor D_0 equal to 2.27×10^{-4} cm^2/s [20]. The average diffusion length L_D of a physisorbed atomic hydrogen is approximated to be half the Si-Si bond length ($L_{\text{Si-Si}} = 1.48$ Å) divided by the fraction of surface that is not hydrogen covered. Using the diffusion coefficient D and the diffusion length L_D we obtain an average surface recombination frequency ν_D. A new random number r_6 is generated to obtain the lifetime of the physisorbed atomic hydrogen τ_D. The lifetime τ_D is then compared to the time of collision between the hydrogen at the surface and an incoming hydrogen atom Δt_H. If $\tau_D < \Delta t_H$, the physisorbed hydrogen atom has enough time to diffuse to a surface dangling bond, releasing an energy of 3.1 eV. In this case, the number of surface hydrogen atoms is updated accordingly. If $\tau_D > \Delta t_H$, the physisorbed hydrogen atom recombines with the incoming radical releasing 4.51 eV. Finally, for high particle temperatures thermal desorption of hydrogen through the Langmuir-Hinshelwood mechanism may occur. This process depends solely on the particle temperature and hydrogen surface coverage [21]. It has an activation energy of 1.86 eV and starts to play a role at temperatures around 900 K. This process removes two hydrogen atoms from the surface, and the energy lost is equal to 1.69 eV for each desorbed hydrogen molecule.

Solution of the time-dependent energy balance requires knowledge of four parameters: the ion density, atomic hydrogen density, electron temperature, and electron density. Two of these parameters, the electron temperature and density, will be determined self-consistently within our model. The other two parameters were determined through experiments to find characteristic values typical for real world plasma situations.

III. EXPERIMENT

In this paper, we address the experimental situation described in detail in [5]. Briefly, the silicon nanocrystals are nucleated and grown in a continuous-flow nonthermal plasma reactor from an argon-silane mixture. The mole fraction of silane is typically between 1% and 2.5%, with the remainder being argon. The discharge is contained in a cylindrical quartz tube with 9 mm inner diameter. The plasma is excited by radio-frequency power of about 80 W coupled to a ring electrode pair. A plasma of a length of 3 – 5 cm is produced in the discharge tube. The typical pressure is 1.4 Torr and the particle residence times in the plasma are a few milliseconds. The mass spectroscopy measurements discussed in [5] indicate that all the input silane is either rapidly converted into particles, or deposited as film on the reactor wall.

A. Ion density measurement

The ion density in the discharge has been experimentally determined using an electrostatic capacitive probe. The capacitive probe technique is ideal for measuring ion fluxes and densities in reactive plasmas [22], since this technique is robust with respect to the probe surface contamination. The probe consists of a wire inserted into the discharge, connected to an external test capacitor and to a rf generator. The rf generator charges the capacitor through the negative self-biasing of the probe to a few tens of volts of potential; the signal from the generator is periodically chopped and the capacitor is discharged because of the positive ion flux from the plasma to the probe. The capacitor's voltage decay rate is a direct measurement of the ion flux to the probe. The measurement has been performed biasing the probe with a frequency of 5 MHz. The probe radius is 0.8 mm, the probe length is 5.5 mm, and the test capacitor has a capacitance of 30 pF. Using relations presented in [22], we measure an ion density of 1.2×10^{11} cm^{-3} for the pure argon discharge. The ion density decreases with increasing concentration of silane, and an ion density of 5×10^{10} cm^{-3} is measured under the typical conditions used to produce the silicon nanocrystals. This value is used for the solution of the particle energy balance.

B. Atomic hydrogen density measurement

For measuring the atomic hydrogen density a corona model was used to interpret the discharge emission spectrum. The corona model's main assumption is that excited states are populated via electron-impact excitation from the ground state and depopulated by radiative deexcitation. Electron impact excitation of metastable states into a higher excited states is not considered in this work. This seems justified as the authors in [23] report that even small concentrations of silane in argon discharges can quench argon metastable

states. Moreover, in [24] direct measurements of the metastable density by optical absorption in an argon-silane plasma showed that the metastable density was below the experimental detection limit of 2×10^{10} cm^{-3}. The population balance of excited states in the corona limit can thus be written as

$$\frac{dn_H^*}{dt} = n_H n_e X_{e,H}(E/N) - n_H^* \sum_i A_i, \quad (11)$$

with n_H the ground-state density and n_H^* an excited state density. n_e is the electron density and $X_{e,H}(E/N)$ is the excitation rate from the ground state, which is a function of the reduced electric field E/N. A_i is the transition probability for the ith optical emission. The values of the transition probabilities for the different energy levels that are considered are obtained from the NIST website [25]. In steady state, we can then rearrange Eq. (11) into the following relation:

$$n_H = \frac{n_H^* \sum_i A_i}{n_e X_{e,H}(E/N)} = \frac{n_H^* A_i \left(\sum_i A_i \Big/ A_i \right)}{n_e X_{e,H}(E/N)} = \frac{I_i 4\pi\lambda_i/hc}{n_e X_{e,H}(E/N)R_i}. \quad (12)$$

I_i is the radiant intensity of the transition i, λ_i is the wavelength of the corresponding transition, h is the Planck constant, c is the speed of light, and R_i is the related branching ratio $A_i/\Sigma_i A_i$. In principle, the atomic hydrogen density can be measured using Eq. (12) after performing an absolute calibration of the detection system. An easier approach is to use line intensity ratios between the hydrogen and argon lines:

$$n_H = n_{Ar} \frac{I_{i,H}\lambda_{i,H}}{X_{e,H}(E/N)R_{i,H}} \frac{X_{e,Ar}(E/N)R_{j,Ar}}{I_{j,Ar}\lambda_{j,Ar}}, \quad (13)$$

where n_{Ar} is the argon background gas density, $I_{i,H}$ is the radiant intensity of the ith transition for hydrogen, $\lambda_{i,H}$ is the wavelength of the ith transition for hydrogen, $I_{j,Ar}$ is the intensity of the jth transition for argon, and $\lambda_{j,Ar}$ is the wavelength of the jth transition of argon. $R_{j,Ar}$ and $R_{i,H}$ are the branching ratios of the respective transitions. $X_{e,H}(E/N)$ and $X_{e,Ar}(E/N)$ are the electron impact excitation rates from the ground states of hydrogen and argon, which are obtained by calculating the electron energy distribution function (EEDF). The EEDF is calculated using the Boltzmann solver based on the local field approximation and the Lorentz expansion into spherical harmonics [26,27]. Cross sections for argon [28,29], helium [30], and atomic [31] and molecular [31,32] hydrogen are included in the calculations, while silane is neglected since it is known that the discharge quickly converts the precursor either into particles or into a film. The Hα hydrogen line at 656.82 nm is chosen for the measurement since it is by far the strongest hydrogen line present in the spectra. For the argon lines, ten different lines corresponding to transitions from the $3p^5 4p$ manifold are selected. These lines are the most intense in the optical emission spectrum of argon. Table I lists the wavelength and energy levels of the considered argon lines. The calculation of the atomic hydrogen density in Eq. (13) is strongly dependent upon the excitation rate $X_e(E/N)$, which in turn is strongly dependent

TABLE I. List of wavelengths and energy levels of the argon lines used for the atomic hydrogen density measurement.

Wavelength (nm)	$E_i - E_j$ (eV)
667.7282	13.4798860 − 11.6235920
696.5431	13.3278562 − 11.5483537
706.7218	13.3022266 − 11.5483537
727.2936	13.3278562 − 11.6235920
738.398	13.3022266 − 11.6235920
750.3869	13.4798860 − 11.8280704
810.3693	13.1531430 − 11.6235920
811.5311	13.0757149 − 11.5483537
826.4522	13.3278562 − 11.8280704
840.821	13.3022266 − 11.8280704

upon the reduced electric field strength E/N, which is unknown. We solve Eq. (13) assuming different values of reduced electric field strength, E/N. The Boltzmann solver is used to calculate the corresponding excitation rate X_e and the corresponding electron temperature T_e, which is obtained as $2/3$ of the mean kinetic energy from the calculated EEDF. For a given electric field strength E/N and electron temperature T_e, we calculate a value of atomic hydrogen density using the line intensity ratio between the Hα line and each argon line in Table I using Eq. (13). We thus obtain a set of atomic hydrogen densities, each value calculated for one of the selected Ar lines. As the atomic hydrogen densities obtained with this procedure differ significantly, we compute the average and the standard deviation. In Fig. 1 we plot this average and standard deviation of the atomic hydrogen densities with respect to the electron temperature. The normalized standard deviation is minimum and equal to 30% for an electron temperature of 4 eV. The atomic hydrogen density corresponding to the optimum electron temperature is equal to 1.7×10^{13} cm^{-3}, which is the value used for the solution of the nanoparticle energy balance. This procedure ensures that the best fit is achieved between the available experimental
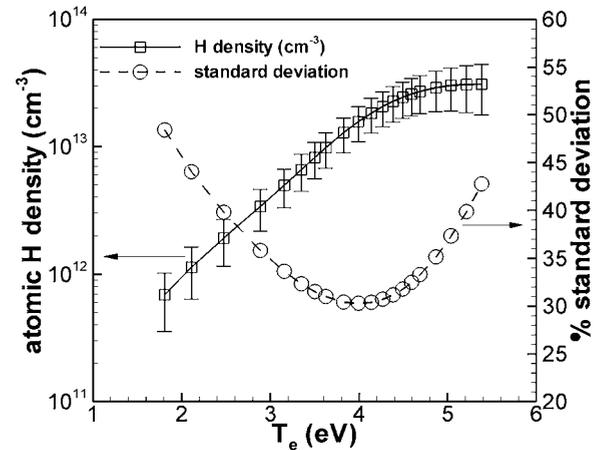

FIG. 1. Atomic hydrogen density and standard deviation of hydrogen densities obtained from different line ratios as a function of electron temperature.

data, i.e., the discharge optical emission spectrum, and the theoretically predicted emission spectrum using the solution of the Boltzmann equation.

C. Electron temperature and electron density calculation

The electron temperature and electron density are determined self-consistently within our model by introducing an ionization term in the electron and ion particle balance. While electron and ions are lost to the particles due to charging events, they are generated in the volume by electron impact ionization. As the ion density was determined experimentally, the ionization rate in the model is changed to maintain a constant ion density equal to the measured value of 5×10^{10} cm^{-3}. A feedback loop within the model adjusts the ionization rate whenever the ion density deviates from the specified value. The relation between electron temperature and ionization rate is known and obtained from the EEDFs obtained from the Boltzmann solver. The electron density is then calculated using the discharge quasineutrality condition:

$$n_e = n_i + n_{\text{particles}} \cdot \bar{Z}, \qquad (14)$$

with $\bar{Z}$ the average number of elementary charges on the particle. The main problem with this approach is that large particle charge fluctuations will induce large fluctuations in ion and electron density, leading to computational instability. Hence, an ensemble of a few hundreds of particles is considered so that the overall charge balance changes slowly in time.

IV. RESULTS AND DISCUSSION

A. Nanoparticle temperature: Size dependence

Initially, simulations were performed for a number of different particle sizes in the limit of low particle concentrations, $n_p \ll n_i$, assuming a gas temperature of 300 K. The particle temperature history for different particle sizes is shown in Fig. 2. The main result of these simulations is that very small particles in a plasma experience a highly unsteady temperature history, with the instantaneous temperature greatly exceeding the background gas temperature. This unsteady behavior is a consequence of the stochastically occurring exothermic events at the particle surface. For small particles these events lead to larger spikes in the particle temperature owing to the particles' small heat capacitance $(4/3)\pi r_p^3 \rho C$. Figure 2 displays the particle temperature history over a period of 1 ms, which is less than the typical residence time of particles in the plasma reactor in Ref. [5]. During this time, several spikes of the particle temperature occur with excess temperatures reaching 700–800 K, i.e., particle temperatures as high as ~1000–1100 K. These particle temperatures are as high as or even exceed the crystallization temperatures for silicon nanocrystals that were reported in Ref. [8].

Figure 2 also shows that the average particle temperature does not depend on particle size, since heating and cooling terms both scale linearly with the particle surface area. The average particle temperature is ~400 K, i.e., about 100 K
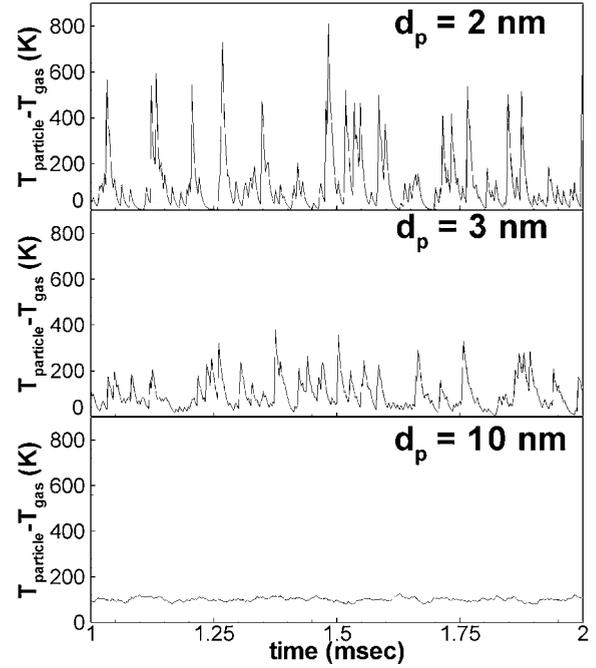

FIG. 2. Excess temperature with respect to the background gas for 2 (top), 3 (middle), and 10 nm (bottom) silicon nanoparticles.

higher than the gas temperature. Given the unsteady temperature of small particles and since the particle temperatures are independent of the temperatures of other particles, it is reasonable to introduce a particle temperature distribution function. We define this particle temperature distribution function (PTDF) as the fraction of time over the simulation length during which the particle maintains a certain excess temperature with respect of the background gas temperature. By definition, the PTDF is normalized to 1 when integrated over all temperatures. The PTDF is shown in Fig. 3 for different particle sizes.

It is clear from Fig. 3 that small particles have significantly higher probabilities of temporarily achieving high temperatures than big particles. Nanoparticles immersed in a
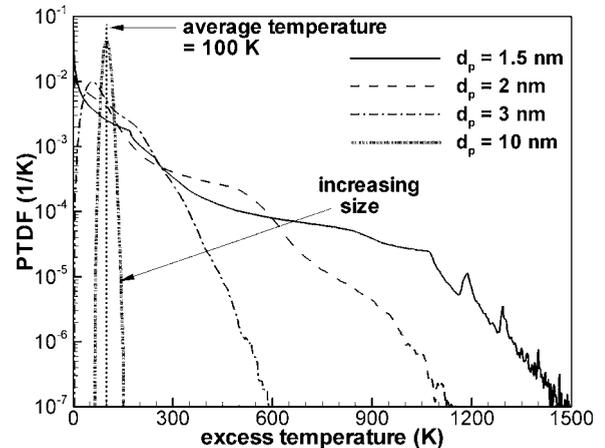

FIG. 3. Particle temperature distribution function as a function of particle size. The average temperature does not depend on the size, and it is equal to +100 K.
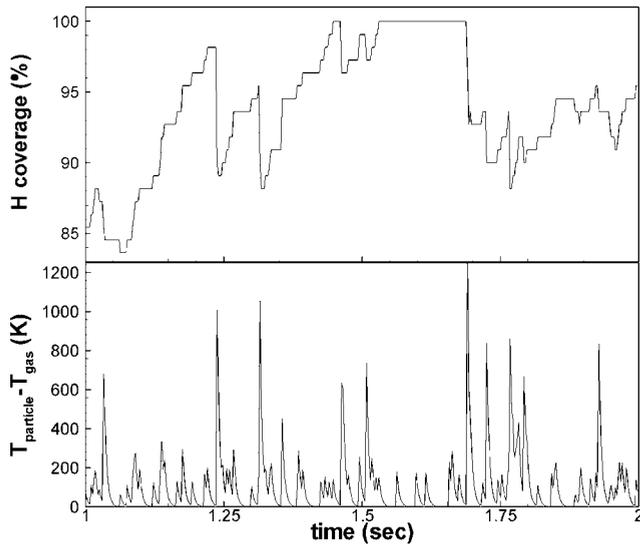
FIG. 4. Temporal evolution of the hydrogen surface coverage and particle temperature for a small particle of 1.5 nm in diameter.

plasma are thus in a significant nonequilibrium with the surrounding gas. The nonequilibrium is more pronounced for small particles, which experience large temperature fluctuation because of their small heat capacitance, and because of the large amount of energy released by the exothermic surface reactions. Under the experimental conditions addressed here, we find that the heating rate due to electron-ion recombination is roughly equal to the one due to surface reactions with atomic hydrogen. Removing atomic hydrogen surface reactions lowers the average excess temperature from ~100 K to ~50 K. However, even in this case the instantaneous particle temperature can still greatly exceed the background gas temperature for short periods of time.

In our model the interaction of atomic hydrogen with the particle surface is modeled as previously described. It is found that a perfect 100% hydrogen coverage is never achieved, because of the finite probability of hydrogen abstraction from the surface [19]. Nevertheless, the hydrogen average surface coverage is always greater than 95%, with a weak dependence of surface coverage on particle size, due to the fact that small particles experience large temperature fluctuations, and thermally activated desorption of hydrogen [21] starts to play a role during large excess temperature peaks. This is shown in Fig. 4 for the case of a 1.5 nm particle. A single electron-ion recombination event can increase the particle temperature to 1000 K, leading to a sudden decrease in hydrogen surface coverage. Between ion recombination events, the flux of hydrogen radicals to the particle quickly restores an almost perfectly hydrogen-terminated surface.

B. Nanoparticle temperature: Volume loading dependence

As already discussed, the presence of small particles in the discharge can catalyze the charge recombination process up to the point where the loss rate of charge carriers to the particles is much larger than the loss to the reactor walls. A series of numerical experiments in which the particle size is
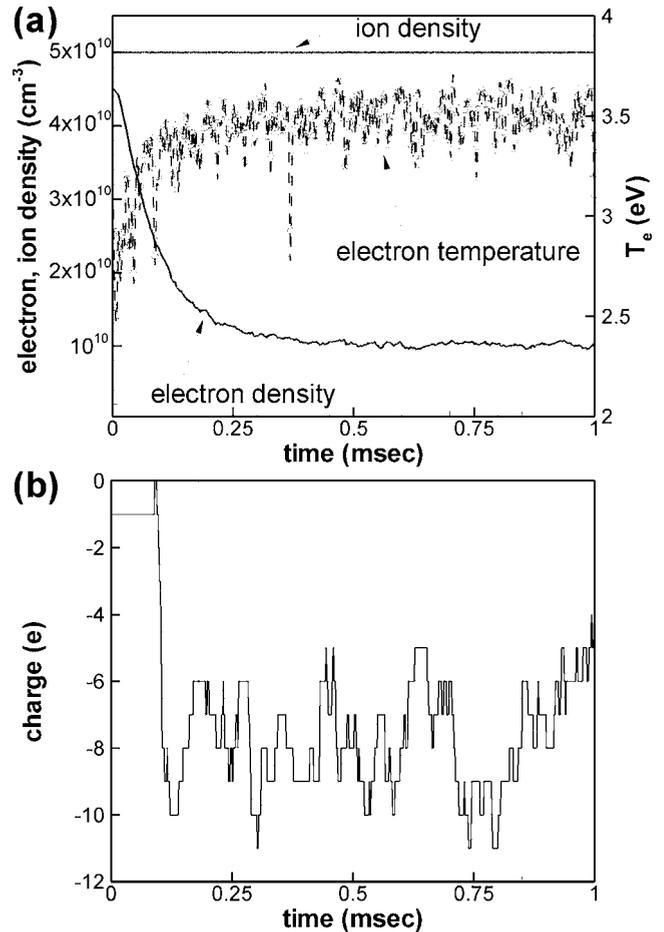

FIG. 5. (a) Start phase of the simulation. Electron temperature is automatically adjusted so that ion density is constant and equal to the specified value. Charging of the particles induces a decrease in electron density. (b) Initial evolution of the charge of a test particle. At $t=0$ the particle charge is set to 1.

kept constant but the particle density is varied will now be presented. The particle size is kept at 5 nm, and the density is varied between 1×10^9 and 3×10^{10} cm^{-3}. Given the stochastic nature of the model and the subsequent fluctuation in the average charge acquired by the particles, numerical instabilities become a problem when particle loadings exceed 3×10^{10} cm^{-3}. As initial condition, the ion density is set equal to the desired value, all the particles are assigned a charge of -1 elementary charge, and the electron density is calculated from the charge balance. Then the time integration is started and a steady state is reached after ~1 ms. The initial phase of the simulation for the case of a particle density of 5×10^9 cm^{-3} is shown in Fig. 5(a). In the initial phase of the simulation, rapid particle charging takes place and the electron density decreases. The ionization rate increases to maintain a constant ion density value, and accordingly the electron temperature increases. The result agrees with the one found in the literature for a similar computational approach [18].

Figure 6(a) shows the particle charge distribution for various particle loadings. The charge distribution was obtained by calculating the fraction of particles that at a certain time
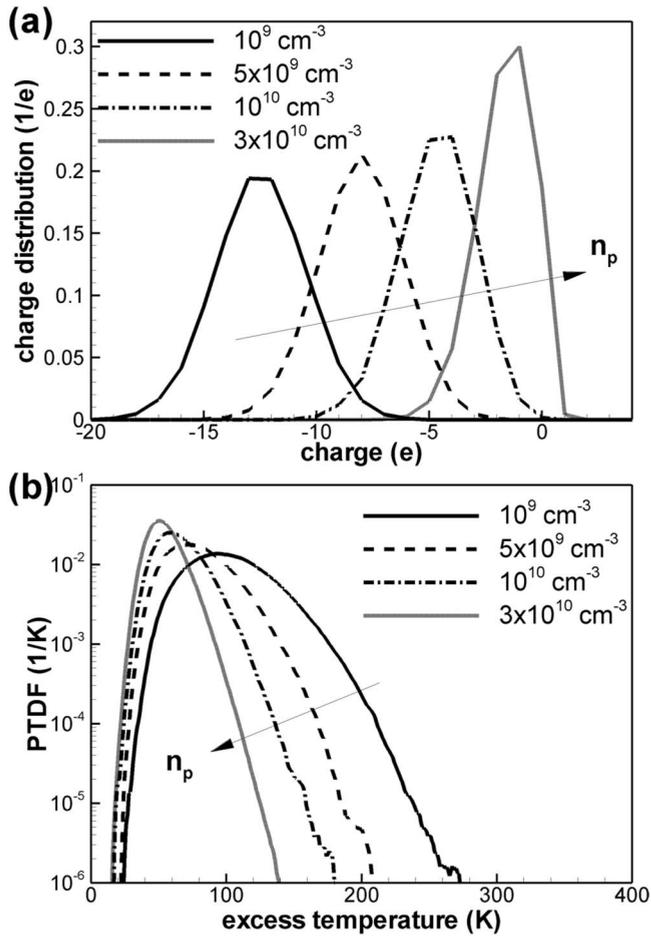
FIG. 6. (a) Particle charge distribution as a function of particle density in the discharge. (b) Temperature distribution of a 5 nm particle as a function of particle density.

step have a given charge, and by averaging over the duration of the simulation, neglecting the initial equilibration phase. As pointed out by Havnes *et al.* [33], the increase in particle density causes a decrease in average negative particle charge. The average number of elementary charges on the particle changes from −11.7 to −1.6 elementary charges when the particle density is changed from 1×10^9 to 3×10^{10} cm^{-3}. The corresponding Havnes parameters P [33] vary between ∼0.1 and ∼2. The reduction of the electron current to the particles leads to a corresponding decrease of the ion collection rate and consequently to a lowering of the particles' heating rate.

It is interesting to see that, for the two highest particle densities, a small fraction of positively charged particles is observed. This is consistent with reports in the literature which have observed particle coagulation frequencies that are larger than those for a neutral aerosol [34], pointing toward the presence of ambipolarly charged particles.

The particle temperature distribution as a function of particle density is shown in Fig. 6(b). With increasing particle density, the probability of finding particles at large excess temperatures decreases rapidly. This is a consequence of the reduced frequency of exothermic surface reactions at the particle surface. This result shows that the particle density in the plasma and particle heating are very closely intertwined. The particle excess temperature, which is ∼100 K for the case of low particle concentration, decreases to an average value of ∼50 K at a density of 3×10^{10} cm^{-3}. The actual particle density for the plasma process discussed in [5], assuming that 50% of the precursor is converted into particles [5], is between 5×10^{10} and 10^{11} cm^{-3} for 5 nm particles. From Fig. 6(b) it appears highly unlikely that particles achieve significant particle temperatures, high enough to actually reach the particles' crystallization temperature. It thus should be expected that particles actually crystallize at smaller sizes, due to both the higher excess temperatures found for smaller particles (see Fig. 3) and the reduced crystallization temperature for smaller particles [8].

V. CONCLUSIONS

In this paper we presented a numerical model describing the energy balance of nanoparticles interacting with a nonthermal plasma. We demonstrated that there is a significant nonequilibrium between the nanoparticle temperature and the background gas temperature and that this phenomenon is particularly pronounced for small particles, whose instantaneous temperature can exceed the gas temperature by several hundreds of kelvins. We also found that the nanoparticle surface, for the case of silicon nanoparticles in an argon-hydrogen plasma, is always almost perfectly terminated by hydrogen even at high particle surface temperatures, due to the significant flux of atomic hydrogen to the particle surface. We also showed that particle temperature and particle charging are strongly coupled and that high particle densities lead to less negatively charged particles and less pronounced nanoparticle heating. We believe that the results of selective heating of nanoparticles essentially explains the formation of nanocrystals of materials with high crystallization temperatures in low-temperature plasmas, whose gas temperature is close to room temperature—an observation which has been a persistent puzzle.

[1] A. Bouchoule, *Dusty Plasmas* (John Wiley & Sons, Chichester, England, 1999).

[2] P. Roca i Cabarrocas, P. Gay, and A. Hadjadj, J. Vac. Sci. Technol. A **14**, 655 (1996).

[3] Y. Ding, Y. Dong, A. Bapat, C. R. Perrey, C. B. Carter, U. R. Kortshagen, and S. A. Campbell, IEEE Trans. Electron Devices **53**, 2525 (2006).

[4] A. Bapat, M. Gatti, Y. Ding, S. A. Campell, and U. Kortshagen, J. Phys. D **40**, 2247 (2007).

[5] L. Mangolini, E. Thimsen, and U. Kortshagen, Nano Lett. **5**, 655 (2005).

[6] L. Mangolini, D. Jurbergs, E. Rogojina, and U. Kortshagen, J. Lumin. **121**, 327 (2006).

[7] L. Mangolini, D. Jurbergs, E. Rogojina, and U. Kortshagen, Phys. Status Solidi C **3**, 3975 (2006).

[8] M. Hirasawa, T. Orii, and T. Seto, Appl. Phys. Lett. **88**, 093119 (2006).

[9] P. Roura, J. Farjas, A. Pinyol, and E. Bertran, Nanotechnology **18**, 175705 (2007).

[10] J. E. Daugherty and D. B. Graves, J. Vac. Sci. Technol. A **11**, 1126 (1993).

[11] G. H. P. M. Swinkels, H. Kersten, H. Deutsch, and G. M. W. Kroesen, J. Appl. Phys. **88**, 1747 (2000).

[12] E. Stoffels, W. W. Stoffels, H. Kersten, G. H. P. M. Swinkels, and G. M. W. Kroesen, Phys. Scr., T **89**, 168 (2001).

[13] A. Bapat, C. Anderson, C. R. Perrey, C. B. Carter, S. A. Campbell, and U. Kortshagen, Plasma Phys. Controlled Fusion **46**, B97 (2004).

[14] A. Barnard and P. Zapol, J. Chem. Phys. **121**, 4276 (2004).

[15] U. Frenzel, U. Hammer, H. Westje, and D. Kreisle, Z. Phys. D: At., Mol. Clusters **40**, 108 (1997).

[16] M. Gatti and U. Kortshagen, Phys. Rev. E **78**, 046402 (2008).

[17] U. Kortshagen and U. Bhandarkar, Phys. Rev. E **60**, 887 (1999).

[18] C. Cui and J. Goree, IEEE Trans. Plasma Sci. **22**, 151 (1994).

[19] D. D. Koleske, S. M. Gates, and B. Jackson, J. Chem. Phys. **101**, 3301 (1994).

[20] M. S. Valipa and D. Maroudas, Appl. Phys. Lett. **87**, 261911 (2005).

[21] K. Sinniah, M. G. Sherman, L. B. Lewis, W. H. Weinberg, J. T. Yates, and K. C. Janda, J. Chem. Phys. **92**, 5700 (1990).

[22] N. S. J. Braithwaite, J. P. Booth, and G. Cunge, Plasma Sources Sci. Technol. **5**, 677 (1996).

[23] L. Sansonnens, A. A. Howling, C. Hollenstein, J. L. Dorier, and U. Kroll, J. Phys. D **27**, 1406 (1994).

[24] A. Bapat, Ph.D. thesis, University of Minnesota, 2007.

[25] http://physics.nist.gov/PhysRefData/ASD/index.html

[26] V. E. Golant, A. P. Zhilinsky, and I. E. Sakharov, *Fundamentals of Plasma Physics* (Wiley, New York, 1980).

[27] U. Kortshagen, H. Schlüter, and A. Shivarova, J. Phys. D **24**, 1571 (1991).

[28] J. Vlcek, J. Phys. D **22**, 623 (1989).

[29] J. E. Chilton, J. B. Boffard, R. S. Schappe, and C. C. Lin, Phys. Rev. A **57**, 267 (1998).

[30] T. Kato and R. Janev, Supplement Journal Nucl. Fusion **3**, 33 (1992).

[31] M. Mitcher and C. Kruger, *Partially Ionized Gases* (Wiley & Sons, New York, 1973).

[32] R. Celiberto, R. K. Janev, A. Laricchiuta, M. Capitelli, J. M. Wadehra, and D. E. Atems, At. Data Nucl. Data Tables **77**, 161 (2001).

[33] O. Havnes, C. K. Goertz, G. E. Morfill, E. Grn, and W. Ip, J. Geophys. Res. **92**, 2281 (1987).

[34] Y. Watanabe, M. Shiratani, H. Kawasaki, S. Singh, T. Fukuzawa, Y. Ueda, and H. Ohkura, J. Vac. Sci. Technol. A **14**, 540 (1996).